ChemSusChem

Chemistry Europe
European Chemical Societies Publishing
ChemSusChem

RESEARCH ARTICLE

Interfacial Electronic Modulation of MoO_2/Fe_3O_4-Melamine Nanorods with Abundant Oxygen Vacancies Towards Large-Current Water Oxidation

Rahmat Ullah[1] | Jinshan Cheng[1] | Sheraz Muhammad[1] | Sumayya Khan[1] | Huaifeng Li[1] | Ali Aman[1] | Ke Zhang[1] | Tayirjan Taylor Isimjan[2] | Shohreh Azizi[3] | Xiulin Yang[1]

[1]Guangxi Key Laboratory of Low Carbon Energy Materials, School of Chemistry and Pharmaceutical Sciences Guangxi Normal University, Guangxi Normal University, Guilin, China | [2]Saudi Arabia Basic Industries Corporation (SABIC) at King Abdullah University of Science and Technology (KAUST), Thuwal, Saudi Arabia | [3]UNESCO-UNISA Africa Chair in Nanosciences/Nanotechnology, College of Graduate Studies, University of South Africa, Pretoria, South Africa

Correspondence: Tayirjan Taylor Isimjan (isimjant@sabic.com) | Shohreh Azizi (azizis@unisa.ac.za) | Xiulin Yang (xlyang@gxnu.edu.cn)

Received: 20 April 2026 | **Revised:** 24 June 2026 | **Accepted:** 17 July 2026

Keywords: electronic modulation | nanorods | oxygen evolution reaction | oxygen vacancy | water oxidation

ABSTRACT

Developing robust, efficient oxygen evolution catalysts is essential to advancing alkaline water electrolysis and sustainable hydrogen production. Herein, we present a vacancy-engineered MoO_2/Fe_3O_4-Mel nanorod composite, grown on nickel foam via a one-step solvothermal strategy. The catalyst possesses abundant oxygen vacancies and strongly coupled MoO_2/Fe_3O_4 heterointerface, while the nitrogen-rich melamine framework promotes electronic modulation of Fe active centers. During electrochemical activation, it undergoes surface reconstruction to generate an FeOOH active phase and oxygen vacancies promote interfacial charge redistribution. These structural and electronic features accelerate charge transfer and facilitate the adsorption and conversion of oxygenated intermediates during oxygen evolution reaction (OER). As a result, the optimized MoO_2/Fe_3O_4-Mel catalyst delivers ultra-low overpotential of 217 mV at 100 mA cm^{-2}, a small Tafel slope of 70 mV dec^{-1}, and maintains stable operation for 150 h. In situ Raman and in situ Fourier transform infrared spectroscopy reveal vacancy-associated surface reconstruction and dynamic oxygenated intermediate evolution, while tetramethylammonium and pH-dependent studies confirm an adsorbate evolution mechanism. A two-electrode MoO_2/Fe_3O_4-$Mel^{(+)}$||$Pt/C^{(-)}$ electrolyzer achieves a low cell voltage of 1.45 V at 100 mA cm^{-2} with negligible degradation over 100 h. This work highlights the effectiveness of interfacial electronic modulation and oxygen vacancy engineering for high-performance alkaline OER catalysts.

1 | Introduction

Hydrogen has received substantial attention as a sustainable alternative to fossil fuels due to its high energy density and zero carbon emission [1, 2]. Electrochemical water splitting provides a sustainable, environmentally friendly approach to hydrogen generation to meet rising energy demands and solve environmental concerns [3, 4]. The hydrogen evolution reaction and oxygen evolution reaction (OER) are the two primary half-reactions in water splitting, with OER being more kinetically challenging and having a significant role in renewable energy conversion technologies [5, 6]. However, its slow multielectron transfer kinetics, along with significant overpotentials, reduce overall efficiency, emphasizing the importance of durable and highly proficient electrocatalysts [7, 8]. Commercial RuO_2- and IrO_2-based catalysts exhibit outstanding intrinsic activity, but their high cost, partial availability, and restricted long-term stability in alkaline environments severely limit their scalability for real-world applications [9, 10]. Therefore, non-noble transition metal-based electrocatalysts have gained popularity as potential and sustainable alternative.

Subsequently, non-precious transition metal oxides like iron oxides (Fe_xO_y) particularly offer Fe centers that readily participate in redox cycling and generate highly active FeOOH species under alkaline OER conditions [11]. However, the OER activity of iron oxides (Fe_xO_y) is often limited by poor electrical conductivity, nonideal intermediate adsorption, and unstable surface reconstruction [12]. Incorporation of secondary metals such as Mo or nitrogen-rich melamine can improve charge transfer, structural stability, and a high density of coordination sites for metal species [13]. The catalytic systems still suffer from nonideal adsorption behavior of oxygenated intermediates and limited accessibility of active sites, affecting the intrinsic activity and durability [14]. Various strategies, including heteroatom doping, defect engineering, interface engineering, and morphology regulation, have been employed to enhance the intrinsic activity and durability of electrocatalysts [15]. Among these methods, oxygen vacancy engineering is recognised as a promising approach for improving the activity and durability of non-precious metal catalysts by tuning local electronic structure and adsorption/desorption energies of major OER intermediates (*OH, *O, and *OOH) [16, 17]. For example, Hua et al. found that the FeOOH nanorods@NiOOH nanosheets with interfacial oxygen vacancies that improved conductivity, controlled Fe-site electronic structures, and promoted oxygen intermediate adsorption, resulting in reduced OER overpotentials (261 mV at 20 mA cm^{-2}) with good stability [5]. Furthermore, Bhattarai et al. reported FeNi-LDH/MIL-88A heterocomposites in which oxygen vacancies tune Fe/Ni active sites, lower O—O bond formation barriers, and promote intermediate adsorption, achieving 200 mA cm^{-2} at 350 mV. Mechanistic studies indicated an AEM-dominated OER pathway, with oxygen vacancies promoting faster reaction kinetics [18]. Similarly, Melamine serves as a structural matrix and coordination platform, enabling efficient Mo incorporation into the Fe_3O_4-Mel system, which generates more oxygen vacancies, modulates the electronic structure, and improves the catalytic activity of the FeOOH active sites. This synergistic effect improves electron transfer, charge transport, and adsorption behavior of oxygenated intermediates, thereby promoting efficient OER. To date, the MoO_2/Fe_3O_4-Mel composite has not been reported, and in this work, we investigate it for the first time as a promising catalyst for high-performance OER.

Herein, we present a MoO_2/Fe_3O_4-Mel composite precatalyst with a nanorod-like morphology, in which alkaline electrochemical activation induces in situ surface reconstruction to form an FeOOH phase. Oxygen vacancies modulate the local electronic environment of Fe centers and optimize the adsorption and transformation of oxygenated intermediates, thereby enhancing OER kinetics. The optimized material, $MoO_{2(0.3)}/Fe_3O_4$-$Mel_{(2)}$, exhibits excellent OER activity with overpotentials of 217 and 259 mV to deliver 100 and 300 mA cm^{-2}, respectively, and demonstrates outstanding durability of 150 h at 100 mA cm^{-2}. *Operando* Raman and *operando* Fourier transform infrared (FTIR) spectroscopy, together with tetramethylammonium (TMA^+) and pH-dependent electrochemical probing, were employed to elucidate the dynamic evolution of the composite precatalyst into the catalytically active FeOOH phase and to establish a clear correlation between oxygen vacancy engineering and catalytic performance. A two-electrode system, MoO_2/Fe_3O_4-$Mel^{(+)}$||$Pt/C^{(-)}$, yields a low cell voltage of 1.45 V at 100 mA cm^{-2} and has a stability of 100 h with minimal voltage decay. Rapid OER kinetics and overall water splitting in alkaline media are collectively facilitated by the nanorod-like morphology and melamine-directed structural features, which improve electron and ion transport. Moreover, oxygen vacancies further activate FeOOH sites and enhance adsorption energies of oxygenated intermediates.

2 | Results and Discussion

2.1 | Synthesis and Characterization of MoO_2/Fe_3O_4-Mel@NF Nanorods

The MoO_2/Fe_3O_4-Mel catalyst was grown on nickel foam (NF) using a one-step solvothermal approach, as illustrated in Figure 1a. MoO_2 was effectively incorporated into Fe_3O_4-Mel, resulting in highly ordered nanorod arrays attached onto the NF substrate. The formation of MoO_2/Fe_3O_4-Mel nanorods proceeds through solvothermal nucleation growth process. During synthesis, Fe and Mo precursor species undergo hydrolysis and interact with melamine through nitrogen-containing functional groups, promoting nucleation and assembly on the Ni foam substrate. Under solvothermal conditions, the Fe and Mo precursors are converted into Fe_3O_4 and MoO_2, respectively. The subsequent growth and interfacial coupling of these phases result in the formation of uniformly distributed MoO_2/Fe_3O_4-Mel nanorods with a strongly coupled heterointerface [19, 20]. X-ray diffraction (XRD) analysis reveals that the composite was successfully developed. The diffraction peaks corresponding to MoO_2 (PDF#96-154–8821), Fe_3O_4 (PDF#96-153-2792), and melamine (CCDC#237082) are closely matched with the standard reference patterns in the $MoO_{2(0.3)}$/Fe_3O_4-$Mel_{(2)}$ sample (Figure 1b). The characteristic diffraction peaks at 31°, 32°, and 34° and 47°–49° correspond to Fe_3O_4, confirming its successful incorporation into the composite. Mo integration increases the diffraction strength associated with Mo-related reflections at roughly 26° and 39°, indicating modest structural modification of the composite framework (Figure S2) [21].

FTIR spectroscopy was used to investigate surface functional groups and bonding conditions (Figures 1c and S3). The absorption spectra at 3350–3450 cm^{-1} are due to N—H stretching vibrations, indicating the existence of surface amine functionalities from melamine [22]. The vibrational bands detected in the 1750–1350 cm^{-1} range correspond to characteristic N—H bending and C—N stretching modes [23]. Notably, the C—N stretching vibration shift, together with the appearance of a metal–oxygen (M–O) vibration near 530 cm^{-1}, indicates notable interactions between the metal oxide components and the melamine framework [24]. Melamine's triazine ring breathing mode, typically located near 810 cm^{-1}, shows a small red shift, indicating metal coordination while maintaining the structural integrity of the melamine scaffold [25]. Ultimately, the XRD and FTIR data demonstrate the effective integration of MoO_2 and Fe_3O_4 into the melamine-based framework while preserving nitrogen-rich coordination conditions favorable to OER catalysis.

Electron paramagnetic resonance (EPR) spectroscopy was applied to study the defect properties and oxygen vacancy generation. As demonstrated in Figure 1d, the MoO_2/Fe_3O_4-Mel composite has a significant signal at $g = 2.04$, which corresponds to the oxygen vacancy-associated unpaired electrons. In comparison,

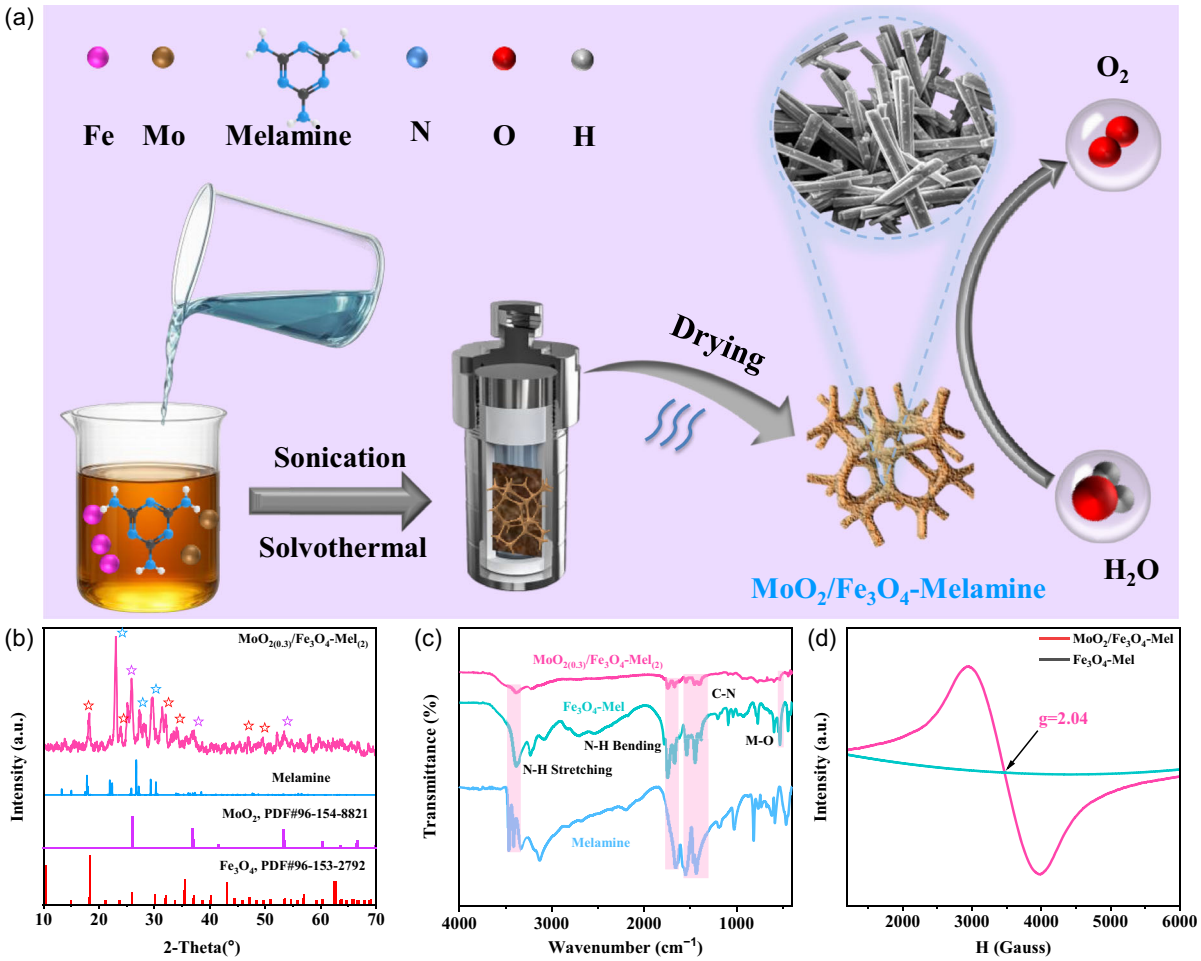

FIGURE 1 | (a) Schematic illustration of the synthesis of MoO_2/Fe_3O_4-Mel. (b) XRD pattern of $MoO_{2(0.3)}/Fe_3O_4$-$Mel_{(2)}$ and simulated pattern of melamine, MoO_2, Fe_3O_4. (c) FTIR spectra of the melamine, Fe_3O_4-Mel and $MoO_{2(0.3)}/Fe_3O_4$-$Mel_{(2)}$. (d) EPR of the Fe_3O_4/Mel and MoO_2/Fe_3O_4-Mel.

the Fe_3O_4-Mel sample shows just a mild and almost insignificant signal [26]. The enhanced oxygen vacancy concentration after Mo addition is attributed to strong interfacial interactions between MoO_2 and Fe_3O_4 generating a heterointerface. Due to difference in electronic structure and local coordination environment, the incorporation of Mo induces lattice distortion and charge redistribution within the heterostructure. To maintain local charge balance and minimize the system energy, oxygen atoms can be preferentially removed from the lattice, leading to the generation of additional oxygen vacancies. Furthermore, the strong interfacial coupling between MoO_2 and Fe_3O_4 may lower the formation energy of oxygen vacancies, thereby facilitating their formation. Consequently, the MoO_2/Fe_3O_4-Mel heterostructure exhibits a strong EPR signal than Fe_3O_4-Mel, indicating a higher concentration of oxygen vacancies [27]. These results endorse that Mo integration efficiently promotes oxygen vacancy development, altering the local electronic environment of Fe active centers and allowing for improved adsorption of OER intermediates.

The morphological features of the catalysts were investigated using scanning electron microscopy (SEM). The Fe_3O_4-Mel sample exhibits irregular flower-like structures, but the MoO_2/Fe_3O_4-Mel composite has consistent nanorod arrays dispersed throughout the NF surface (Figures 2a,b and S1a–e) [28]. The significant morphological conversion seen following Mo integration proposes that MoO_2 plays an important role in driving structural progression during solvothermal growth. Transmission electron microscopy (TEM) supports the production of well-defined 1D nanorod structures in MoO_2/Fe_3O_4-Mel (Figure 2c). The selected area electron diffraction (SAED) patterns show discrete concentric diffraction rings, which indicate that the composite material is polycrystalline (Figure 2d) [29]. The indexed diffraction lines correspond to the (224) planes of Fe_3O_4 and (212) planes of MoO_2, confirming the presence of both phases in the composite. High-resolution TEM (HRTEM) images expose clearly determined lattice fringes with interplanar spacings of 0.108 and 0.163 nm, consistent to the (112) plane of MoO_2 and the (231) plane of Fe_3O_4, respectively (Figure 2e). The presence of continuous and well-defined lattice fringes confirms high crystallinity and demonstrates intimate interfacial coupling between the multiphase components within the composite (Figure 2f) [30]. The significant morphology evolution from Fe_3O_4-Mel to MoO_2/Fe_3O_4-Mel indicates that Mo incorporation has strong effect on crystal growth during the synthesis process. XRD, SAED, and HRTEM analyses confirm the coexistence of MoO_2 and Fe_3O_4 within the heterostructure. The morphology of pristine Fe_3O_4, comprising small particles, is shown in Figure S1a. Based on the reported morphology of solvothermally synthesized MoO_2 systems, the observed nanorod architecture is likely associated with the Mo-containing domains, while the

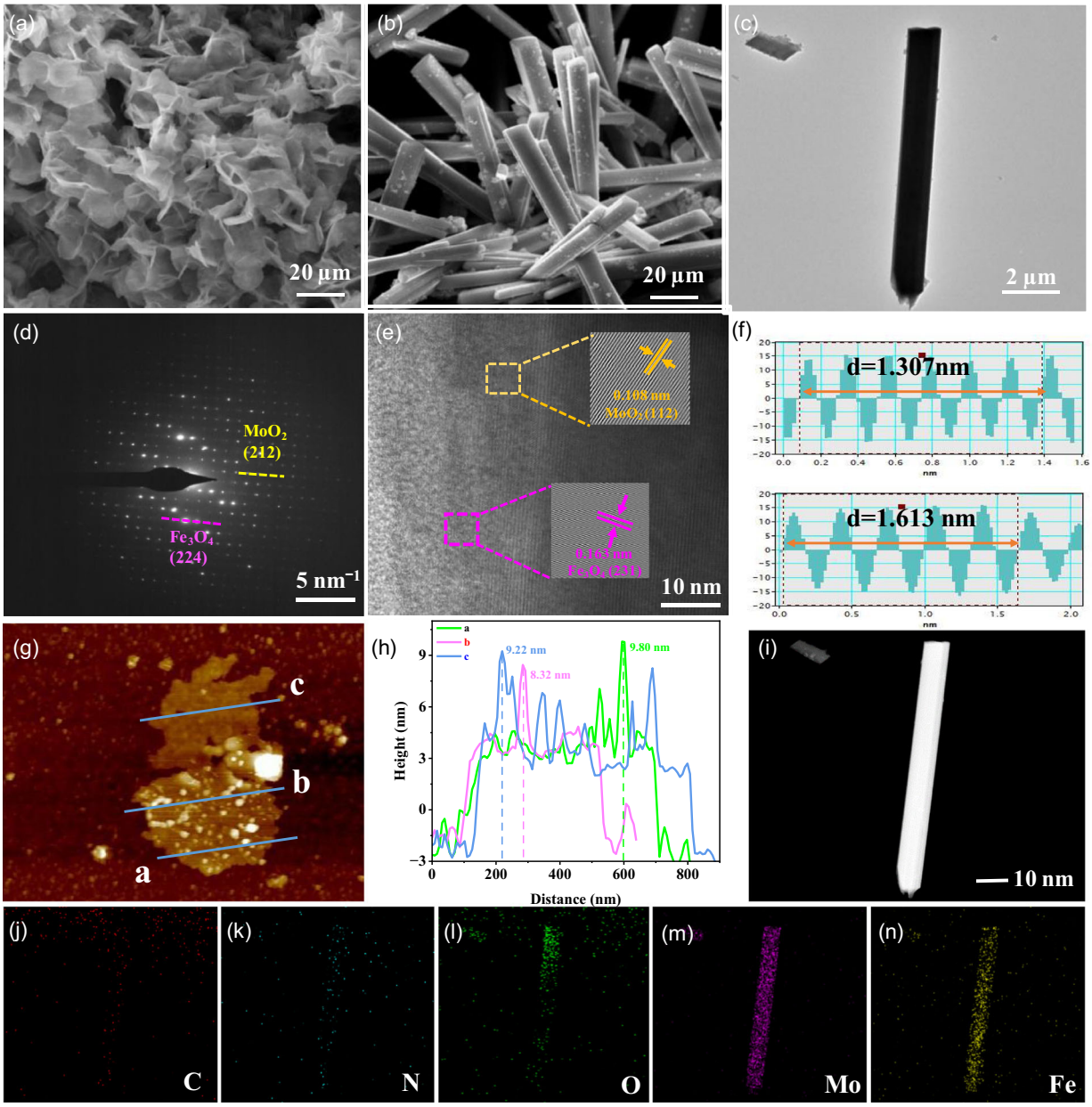

FIGURE 2 | SEM images of (a) Fe_3O_4-Mel and (b) MoO_2/Fe_3O_4-Mel. (c) TEM image of MoO_2/Fe_3O_4-Mel. (d) SAED pattern. (e) HR-TEM image. (f) The lattice fringe profiles of the indicated areas. (g) AFM. (h) Corresponding height profiles from AFM. (i–n) HAADF–STEM image and the corresponding elemental mappings of C, N, O, Mo, and Fe for the MoO_2/Fe_3O_4-Mel composite.

uniformly dispersed Fe_3O_4 nanoparticles contribute to the formation of a strongly coupled heterointerface [31, 32].

Atomic force microscopy (AFM) analysis of MoO_2/Fe_3O_4-Mel reveals well-defined nanorod-like structures with an average thickness of ≈9.11 nm (Figure 2g,h). These uniformly distributed nanorods exhibit regular 1D morphology with high aspect ratios, providing large exposed surface areas and well-defined directional transport channels within the composite [33]. The hierarchical nanostructure of the MoO_2/Fe_3O_4-Mel catalyst is further confirmed by high-angle annular dark-field scanning transmission electron microscopy (HAADF–STEM) imaging (Figure 2i). The complementary energy-dispersive X-ray spectroscopy spectra (Figure S4) and elemental mapping (Figure 2j–n) show a relatively uniform distribution of Fe, Mo, O, N, and C throughout the composite, promoting effective interfacial charge transfer, thereby enhancing OER catalytic performance.

High-resolution X-ray photoelectron spectroscopy (XPS) was executed to study the surface chemical composition, valence states, and electronic atmospheres of Fe_3O_4-Mel@NF, MoO_2/Fe_3O_4@NF and MoO_2/Fe_3O_4-Mel@NF composite. The survey spectrum (Figure S7) shows the existence of C, O, N, Mo, and Fe elements. The high-resolution Fe 2p spectrum of MoO_2/Fe_3O_4-Mel (Figure 3a) composite exhibits discrete Fe $2p_{3/2}$ and Fe $2p_{1/2}$ peaks, which are accompanied by distinctive satellite characteristics. Peaks located at 710.2 and 721.0 eV belong to Fe^{2+}, whereas peaks at 713.2 and 723.5 eV correspond to Fe^{3+} states, suggesting the coexistence of mixed-valence iron species within the composite [34]. Fe-related satellite peaks appear at 716.8 and

726.0 eV. Notably, the Fe^{2+} related peak in the MoO_2/Fe_3O_4-Mel@NF and MoO_2/Fe_3O_4 are identical and exhibit a positive shift of ≈0.18 eV compared with Fe_3O_4-Mel@NF, suggesting modulation of the Fe electronic environment induced by Mo incorporation. Quantitative analysis of Fe species (Figure 3b) further reveals significant variation in the Fe^{2+}/ Fe^{3+} following Mo integration. The Fe^{2+} and Fe^{3+} content of the Fe_3O_4-Mel/NF sample are 14.7 and 43 %, respectively, whereas the MoO_2/Fe_3O_4-Mel@NF composite shows increased Fe^{2+} content (29.6%) and slightly elevated Fe^{3+} content (45 %). The altered Fe oxidation-state distribution suggests that Mo-induced defect formation facilitates dynamic Fe redox transitions, thereby increasing the population of electrochemically active Fe^{3+} sites favorable for OER catalysis [35].

The high-resolution Mo 3d XPS spectrum of the MoO_2/Fe_3O_4-Mel and MoO_2/Fe_3O_4 composite (Figures 3c and S6) exhibits two sets of spin–orbit doublets corresponding to Mo $3d_{5/2}$ and Mo $3d_{3/2}$ states, which show a positive shift (~0.20 eV) when melamine is incorporated. The peaks located at 232.80 and 235.09 eV are attributed to Mo^{6+} species, whereas additional peaks at 231.77 and 234.72 eV correspond to Mo^{4+} species, indicating partial surface oxidation of Mo species [36]. The coexistence of Mo^{4+} and Mo^{6+} confirms the presence of mixed-valence Mo states, suggesting strong electronic interactions and charge redistribution at the Mo—O—Fe heterointerface, which likely contribute to catalytic modulation. The shifting of Mo^{6+} peak after melamine incorporation indicates strong interaction between Mo and N of melamine.

Similarly, the O 1s XPS spectrum of the MoO_2/Fe_3O_4-Mel composite (Figure 3d) can be deconvoluted into three distinct components. The peak at ≈530.29 eV corresponds to lattice oxygen associated with Mo—O and Fe—O bonds. The peak near 531.03 eV is attributed to oxygen vacancy-related defects, while the peak at 532.6 eV corresponds to surface-adsorbed water species [35, 37]. These XPS findings are consistent with EPR spectroscopy, which exhibits stronger signal for Mo-containing sample, characteristic of unpaired electrons in oxygen vacancy defects. The corresponding MoO_2/Fe_3O_4 heterostructure also has similar peaks and peak position is also same as MoO_2/Fe_3O_4-Mel. Quantitatively, the O 1s XPS spectra of MoO_2/Fe_3O_4-Mel and MoO_2/Fe_3O_4 indicate an equal concentration of oxygen-vacancy peak (~50.5%) but the quantity of O_{ads} peak is increased from 16.2% to 20.9% (Figure 3e). This O_v-related peak is absent in Fe_3O_4-Mel, which instead exhibits corresponding OH peaks, indicating that vacancy is induced by MoO_2 incorporation into Fe_3O_4 environment, forming a heterointerface. This concurrent increase in XPS signal and defect-sensitive EPR signal provides strong evidence that Mo incorporation increases the concentration of oxygen vacancies in the catalyst. These oxygen vacancies, combined with Mo—Fe electronic coupling, regulate

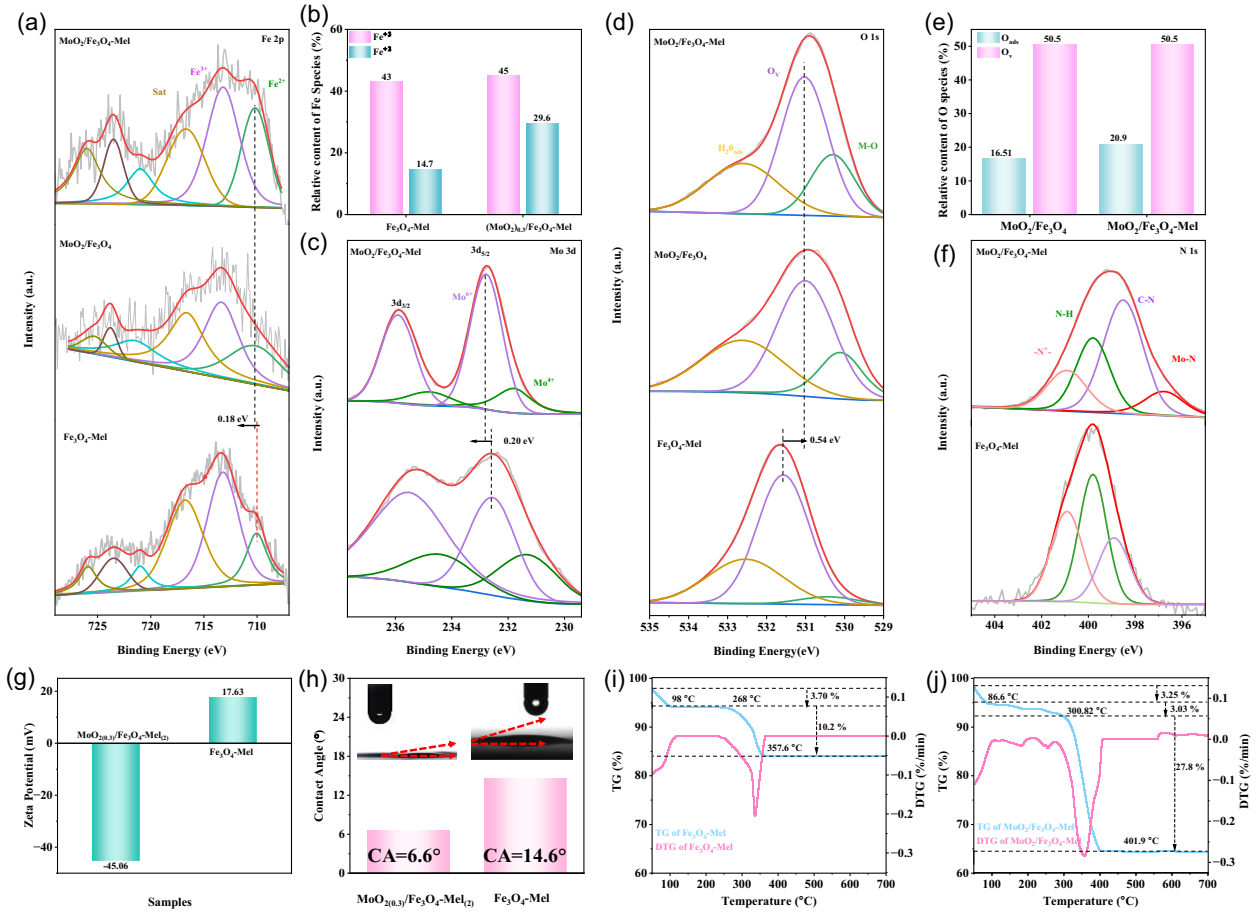

FIGURE 3 | High-resolution XPS spectra of Fe_3O_4-Mel, MoO_2/Fe_3O_4, and MoO_2/Fe_3O_4-Mel. (a) Fe 2p. (b) Relative distribution of Fe^{2+} and Fe^{3+} species. (c) Mo 3d. (d) O 1s. (e) Relative % age of O_{ads} and O_v in MoO_2/Fe_3O_4 and MoO_2/Fe_3O_4-Mel. (f) N 1s. (g) Zeta potentials. (h) Contact angle (CA) of prepared catalysts and thermal characterization. (i,j) TG/DTG curves of Fe_3O_4-Mel and MoO_2/Fe_3O_4-Mel.

the local electronic environment and facilitate the catalytic process.

The N 1s spectrum of MoO_2/Fe_3O_4-Mel (Figure 3f) can be deconvoluted into four peaks. The peak located at ≈396.76 eV corresponds to Mo—N coordination, indicating strong interfacial interactions between Mo species and the melamine matrix [38]. Peaks centered at 398.52 and 399.80 eV correspond to C—N and N—H bonding environments, respectively, while the peak near 400.96 eV is assigned to graphitic or protonated nitrogen species that enhance electronic conductivity [39]. The C—N peak in the MoO_2/Fe_3O_4-Mel exhibits a noticeable binding energy shift relative to Fe_3O_4-Mel, further supporting electronic interactions between Mo species and nitrogen-containing ligands. In contrast, the Fe_3O_4-Mel shows only three distinct nitrogen-related species without observable Mo—N bonding, confirming that Mo incorporation introduces additional metal-nitrogen coordination that facilitates interfacial electronic exchange [40]. The C 1s spectrum of MoO_2/Fe_3O_4-Mel (Figure S5) has three major peaks located at 284.6, 286.5, and 288.5 eV, corresponding to C—C/C═C, C—/C—N, and C═O bonding configurations, respectively [40]. The nitrogen-rich melamine framework promotes the formation of a strongly coupled MoO_2/Fe_3O_4 heterointerface during synthesis and growth. The binding energy shifts observed in the Mo 3d and Fe 2p XPS spectra of the MoO_2/Fe_3O_4-Mel catalyst indicate interfacial electronic modulation induced by melamine. These results suggest that melamine serves as an interfacial structural and electronic modulator in coordination with MoO_2/Fe_3O_4 heterointerface.

The role of oxygen vacancy defects in interfacial electronic modulation in MoO_2/Fe_3O_4-Mel was investigated by EPR and comprehensive XPS studies. Both of these techniques confirm the presence of oxygen vacancy defects in MoO_2/Fe_3O_4-Mel. Compared with Fe_3O_4-Mel, the O 1s spectrum of MoO_2/Fe_3O_4-Mel exhibits shift in the M—O, O_v, and O_{ads} components, indicating a modified local oxygen environment after heterostructure formation. Although the O_v concentration remains nearly unchanged (50.5 %) compared with MoO_2/Fe_3O_4 in comparative XPS analysis, the Mo 3d spectra display a distinct positive B.E shift (~0.20 eV), indicating sufficient electron redistribution across Mo—O—Fe interface. This oxygen vacancy environment also causes increase in O_{ads} peak concentration percentage with incorporation of melamine (Figure 3e). Consequently, the electronic modulation of active sites is achieved, accelerating charge transfer, and promoting the formation of reaction intermediates during the catalytic process.

Zeta potential (ζ) measurements support these findings. The MoO_2/Fe_3O_4-Mel composite has a much higher negative surface potential (−45.06 mV) than Fe_3O_4-Mel (17.63 mV), suggesting stronger electrostatic attraction toward OH^- species and better electrolyte–catalyst interactions (Figure 3g) [41]. Surface wettability analysis using water contact angle measurements (Figure 3h) demonstrates that the MoO_2/Fe_3O_4-Mel electrode has a very low contact angle of 6.6°, indicating greater hydrophilicity over Fe_3O_4-Mel (14.6°). The improved wettability enhances electrolyte penetration, promotes rapid mass transfer across the electrode–electrolyte interface, and promotes superior electrochemical performance [42].

Thermogravimetric analysis and derivative thermogravimetry (DTG) show significant modifications in the thermal properties of Fe_3O_4-Mel and MoO_2/Fe_3O_4-Mel composites (Figure 3i,j). The removal of physically adsorbed water molecules from the catalyst surface causes an initial weight loss of roughly 3.70% in Fe_3O_4-Mel at temperature approaching 98 °C. This is followed by a subsequent weight loss of 10.2%, centered at ≈357.6 °C, which corresponds to organic species degradation and the partial structural rearrangement of the composite. The successive weight loss at higher temperatures is predominantly related to degradation of the melamine framework and eventual collapse of the composite matrix [43]. In comparison, MoO_2/Fe_3O_4-Mel has significantly higher thermal stability. The composite loses less weight (3.25%) at low-temperature region (≈86.6 °C), indicating less moisture adsorption and improved structural compactness. This is followed by a modest breakdown event (3.03%) at 300.82 °C, which involves the destruction of residual organic moieties. At around 401.9 °C, there is a major weight loss of 27.8%, indicating the delayed structural decomposition as compared to Fe_3O_4-Mel. More significantly, the main disintegration process begins at a higher temperature and progresses more slowly, reflecting the enhanced thermal resistance of the composite [44].

The higher thermal stability of MoO_2/Fe_3O_4-Mel might be attributed to superior interfacial coupling and electronic interactions between MoO_2, Fe_3O_4, and the melamine-based nitrogen-rich framework. Such extensive interfacial integration increases lattice rigidity and defect stabilization, predominantly oxygen vacancy retention, which is required for catalytic activity. Catalytically, improved thermal stability is strongly connected with structural robustness during electrochemical operation. Under alkaline OER conditions, Fe-based precatalysts often undergo dynamic surface reconstruction, resulting in catalytically active FeOOH phases. The improved structural integrity of MoO_2/Fe_3O_4-Mel allows for regulated and sustained reconstruction, limiting quick catalyst degradation or active site loss during long-term operation. Furthermore, the strong composite framework enables stable electronic interactions between Mo and Fe centers, which promotes reversible Fe valence transitions and stabilizes oxygen vacancy defects during catalytic cycling. This structural durability contributes to the preservation of active site density and effective charge transfer pathways under harsh oxidative situations. As a result, the increased thermal stability of MoO_2/Fe_3O_4-Mel provides significant evidence for its improved electrochemical durability and maintained catalytic effectiveness during long-term OER operation [45].

2.2 | Electrocatalytic OER Performance

The OER catalytic performance of the synthesized catalysts was evaluated in 1.0 M KOH using a conventional three-electrode configuration. All potentials were referenced to the reversible hydrogen electrode (RHE), and current densities were fully iR-compensated. Linear sweep voltammetry (LSV) was employed to systematically assess OER activity in alkaline media (Figure 4a). The $MoO_{2(0.3)}/Fe_3O_4$-$Mel_{(2)}$ catalyst exhibits outstanding electrocatalytic performance, requiring low overpotentials of 217 and 259 mV to achieve current densities of 100 and 300 mA cm^{-2}, respectively, surpassing Fe_3O_4-Mel, MoO_2/Fe_3O_4, and benchmark RuO_2 under identical conditions (Figure 4b). Optimization studies

involving Mo and melamine loading further confirm the superior catalytic performance of the optimized composition (Figure S8a,b). Comparative analysis with previously reported OER catalysts demonstrates that the performance of $MoO_{2(0.3)}/Fe_3O_4$-$Mel_{(2)}$ ranks favorably among state-of-the-art catalysts operating under similar conditions (Figure 4d and Table S1).

Tafel slope analysis derived from polarization curves provides insight into OER reaction kinetics (Figure 4c). $MoO_{2(0.3)}/Fe_3O_4$-$Mel_{(2)}$ exhibits a low Tafel slope of 70 mV dec^{-1}, which is significantly smaller than those of Fe_3O_4-Mel (91 mV dec^{-1}), MoO_2/Fe_3O_4 (81 mV dec^{-1}), and RuO_2 (140 mV dec^{-1}), indicating accelerated reaction kinetics. The improved kinetics can be attributed to electronic modulation of Fe active centers induced by Mo incorporation and oxygen vacancy formation, which optimize adsorption energetics of oxygenated intermediates during the OER process. Mass activity analysis further highlights the intrinsic catalytic efficiency of the materials (Figure 4f). $MoO_{2(0.3)}/Fe_3O_4$-$Mel_{(2)}$ delivers the highest mass activity of 77.33 A g^{-1}, confirming its superior intrinsic catalytic performance relative to the comparison catalysts [46].

Cyclic voltammetry was performed to estimate the electrochemically active surface area (ECSA). As shown in Figure S9a–c and Figure 4g, $MoO_{2(0.3)}/Fe_3O_4$-$Mel_{(2)}$ exhibits the highest double-layer capacitance ($C_{dl} \approx 38.83$ mF cm^{-2}) among all samples. The corresponding ECSA value of 970.75 cm^2 indicates a high density of accessible catalytically active sites (Figure 4h). This enhancement originates from the hierarchical nanorod architecture and strong metal–melamine interfacial interactions, which promote efficient exposure of active centers and facilitate electrolyte accessibility.

Electrochemical impedance spectroscopy (EIS) was employed to investigate the properties of charge transfer and intrinsic

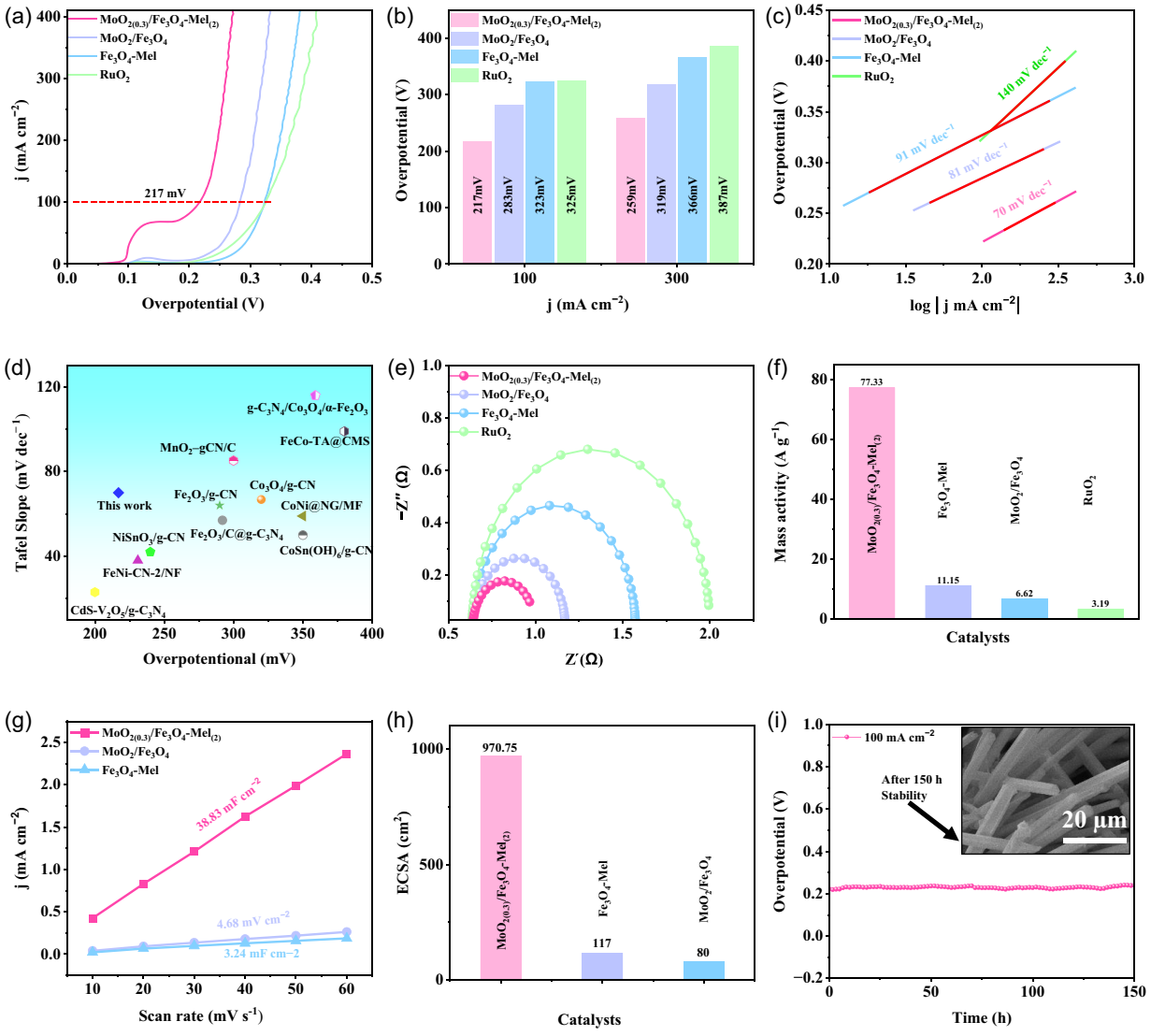

FIGURE 4 | OER performance of various electrocatalysts in 1.0 M KOH solution. (a) LSV polarization curves of the catalysts. (b) Comparison of overpotential at 100 and 300 mA cm^{-2}. (c) Corresponding Tafel slopes. (d) Comparison of the overpotential and Tafel slope with previously reported OER catalysts. (e) Electrochemical impedance spectroscopy (EIS). (f) Relative mass activity. (g) C_{dl} plots. (h) ECSA comparison. (i) Long-term stability test of the catalyst at 100 mA cm^{-2}, with the inset showing SEM image of the corresponding catalyst after 150 h stability.

electrical conductivity of the catalysts. The Nyquist plots provide insight into interfacial electron transfer behavior: smaller semicircle diameters correspond to lower charge–transfer resistance (R_{ct}) and faster electron transport kinetics. As shown in Figure 4e, $MoO_{2(0.3)}/Fe_3O_4$-$Mel_{(2)}$ exhibits the lowest R_{ct} value (~0.35 Ω), which is significantly smaller than those of MoO_2/Fe_3O_4 (~0.53 Ω), Fe_3O_4-Mel (~0.93 Ω), and RuO_2 (~1.35 Ω). The reduced R_{ct} value indicates superior interfacial charge transfer capability, which can be attributed to synergistic Mo—Fe electronic interactions and oxygen vacancy-induced electronic delocalization. These features collectively facilitate efficient electron migration across the catalyst–electrolyte interface and accelerate OER kinetics. Long-term electrochemical durability was evaluated using chronopotentiometric (CP) testing. The $MoO_{2(0.3)}/Fe_3O_4$-$Mel_{(2)}$ catalyst maintains stable operation at a current density of 100 mA cm^{-2} for 150 h with negligible performance degradation (Figure 4i), demonstrating excellent operational stability under alkaline OER conditions. The outstanding durability is attributed to the robust composite architecture, strong interfacial coupling, and vacancy-stabilized active sites, which enable sustained catalytic reconstruction and prevent structural degradation during prolonged electrochemical operation.

The OER performance is attributed to the synergistic effect of oxygen vacancies and interfacial electronic modulation. The oxygen vacancies provide defect sites that facilitate OH^- adsorption and increase the concentration of surface-adsorbed oxygen species, while the coupled Mo—O—Fe heterointerface promotes charge redistribution and accelerates electron transfer kinetics. The combined effect optimizes the adsorption/desorption of oxygenated intermediates, resulting in intrinsic activity of the catalytic sites.

2.3 | *Operando* Spectroscopic Analysis

The electrochemical redox dynamics of active metal centers drive active catalyst surface reconstruction during OER, generating highly active sites that enhance oxygen evolution performance. To probe these dynamic interfacial processes under operating conditions, in situ EIS was used to monitor charge transfer behavior and surface activation. With increasing applied potential, a progressive decrease in phase angle is observed (Figure 5a,b), indicating accelerated reaction kinetics and enhanced adsorption of oxygenated intermediates [47]. The complete transition for MoO_2/Fe_3O_4-Mel is observed at an onset potential of 1.50 V, significantly lower (50 mV lower) than that of Fe_3O_4-Mel, for which the transition is delayed and occurs around 1.55 V, highlighting the enhanced kinetics of the MoO_2/Fe_3O_4-Mel catalyst. Notably, MoO_2/Fe_3O_4-Mel exhibits consistently lower phase angles compared to Fe_3O_4-Mel, suggesting more efficient interfacial charge transfer and faster surface reconstruction. Additional insights are obtained from EIS-derived Bode plots (Figure 5c). The prominent features observed in the low-frequency domain (10^{-2}–10^{1} Hz) are associated with OER-related charge transfer processes, whereas the peaks in the high-frequency region (10^{2}–10^{5} Hz)

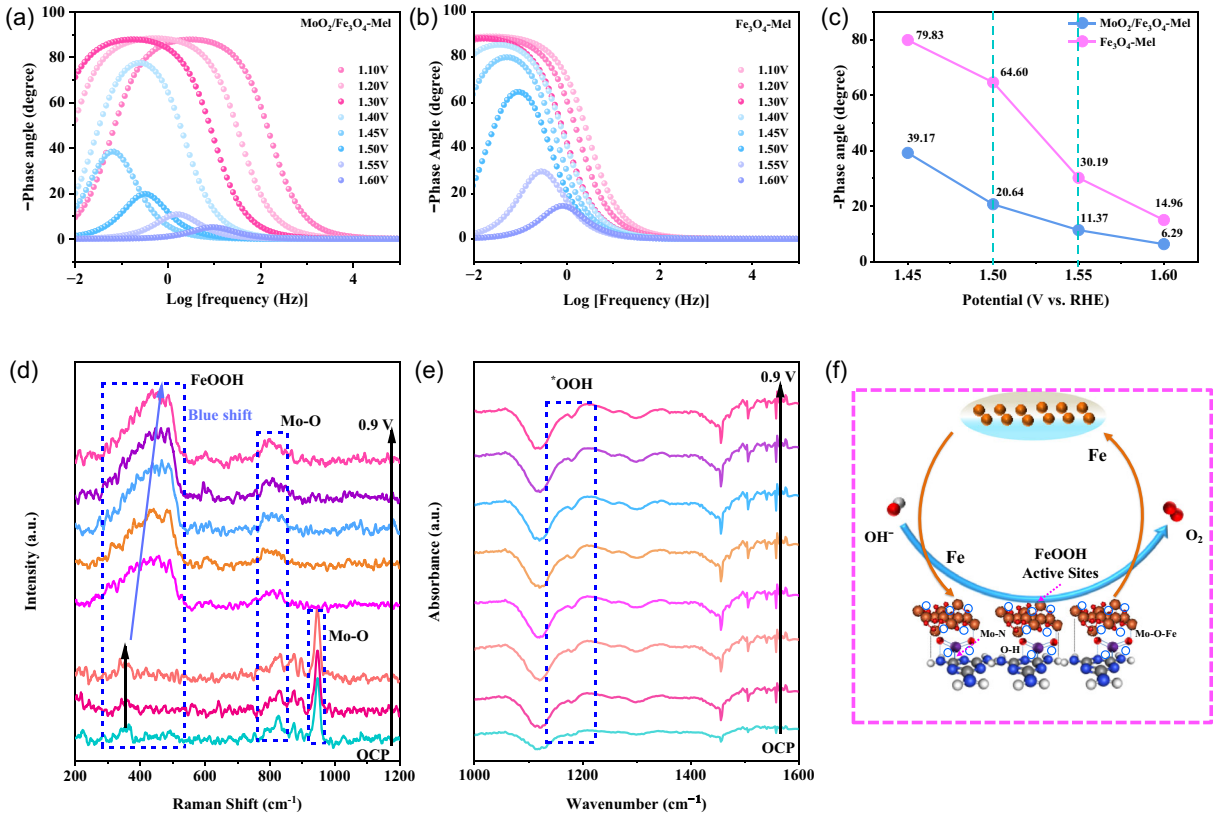

FIGURE 5 | Bode plots of (a) MoO_2/Fe_3O_4-Mel (b) Fe_3O_4-Mel at different applied potentials (vs. RHE). (c) Phase angle response as a function of applied potential for MoO_2/Fe_3O_4-Mel and Fe_3O_4-Mel. (d) Potential-dependent *Operando* Raman spectra of MoO_2/Fe_3O_4-Mel@NF at different potentials (vs. RHE). (e) *Operando* FTIR spectra of MoO_2/Fe_3O_4-Mel@NF at different potentials. (f) Oxygen Vacancy modulated FeOOH reconstruction on MoO_2/Fe_3O_4-Mel nanorods.

correspond to redox transitions of Fe species. The consistently reduced phase angles of MoO_2/Fe_3O_4-Mel across these frequency domains confirm enhanced electron transport efficiency and reduced interfacial resistance, collectively promoting faster catalytic kinetics and improved OER performance [48, 49]. Overall, the in situ EIS results demonstrate that Mo incorporation effectively modulates the electronic environment of Fe active centers, thereby significantly improving catalytic performance by accelerating charge transfer kinetics and improving structural stability during electrochemical operation.

To further elucidate the dynamic structural evolution of the catalyst, *operando* Raman spectroscopy was performed across a potential range from open-circuit potential (OCP) to 0.9 V (vs. RHE). At low potentials, the catalyst retains its original structural features, indicating stable coordination environments of Mo—O and Fe—O bonds prior to OER onset (Figure 5d). Upon increasing the applied potential, gradual weakening and broadening of vibrational modes are observed, suggesting lattice distortion and oxygen rearrangement under anodic polarization. At elevated potentials (after 0.2 V), blue shift occurs and Raman bands emerge in the 350–550 cm^{-1} region, corresponding to the E_g bending and A_{1g} stretching modes of Fe—O vibrations in FeOOH. These spectral features confirm in situ oxidation of Fe^{2+} to Fe^{3+} and dynamic surface reconstruction into catalytically active FeOOH phases [50, 51]. Additionally, Raman bands observed in the 750–870 and 930–970 cm^{-1} regions are attributed to bridging Mo—O vibrational modes associated with transient MoO_x species generated under alkaline OER conditions [52]. The gradual attenuation of these bands during extended operation suggests partial Mo leaching and progressive surface restructuring [53, 54]. Importantly, the observed gradual phase evolution, rather than abrupt structural transformation, indicates that oxygen vacancies play a critical role in lowering the energetic barrier for Fe—O bond reconstruction and facilitating formation of highly active FeOOH species [55].

Operando FTIR spectroscopy was conducted to investigate surface reaction intermediates under OER-relevant potentials (Figure 5e). At OCP, negligible absorption features are observed, indicating minimal intermediate adsorption on the catalyst surface. Upon application of anodic potentials within the OER region, characteristic absorption bands appear in the 1140–1220 cm^{-1} range, which are assigned to OOH intermediates [56, 57]. The progressive emergence and intensification of these bands indicate efficient formation and conversion of oxygenated intermediates during OER on the reconstructed catalyst surface. Notably, the MoO_2/Fe_3O_4-Mel@NF electrode exhibits significantly stronger intermediate-related signals, particularly for OOH species, which is attributed to the high density of oxygen vacancies, providing electron-rich adsorption sites [58, 59]. These results demonstrate that oxygen vacancies not only enhance intermediate adsorption but also facilitate intermediate transformation by lowering activation barriers.

Based on the combined *operando* spectroscopic observations, the OER mechanism on MoO_2/Fe_3O_4-Mel@NF is strongly governed by oxygen vacancy engineering. Oxygen vacancies act as preferential adsorption sites for OH^- ions, enabling rapid formation of *OH species while stabilizing the high valence Fe^{3+} within FeOOH active phases, thereby accelerating OER reaction kinetics and improving overall catalytic efficiency (Figure 5f).

2.4 | Post CP Analyses and Mechanistic Investigation

SEM images obtained after CP testing (Figure S10) reveal that the catalyst maintains its original nanorod morphology without noticeable structural degradation, confirming excellent morphological stability during prolonged OER operation. XPS analysis performed after extended CP further provides insights into dynamic surface reconstruction and defect evolution. The Fe 2p spectrum exhibits a pronounced shift toward higher binding energies, indicating enrichment of Fe^{3+} species, which is characteristic of FeOOH formation under OER conditions (Figure 6a) [60]. Concurrently, the O 1s spectrum shows increased contribution from defect-related oxygen species, accompanied by a shift toward lower binding energies (Figure 6c). These signals are typically associated with oxygen vacancies and surface hydroxyl species, which play a critical role in enhancing catalytic activity by promoting OH^- adsorption and facilitating charge transfer across the electrode–electrolyte interface.

Meanwhile, the Mo 3d spectrum reveals gradual attenuation of Mo-related signals after CP testing, indicating partial dissolution or leaching of Mo species during electrochemical operation (Figure 6b). The N 1s spectrum exhibits moderate signal attenuation, suggesting partial oxidation of the melamine framework while preserving its structural integrity and electronic modulation capability. The corresponding Mo—N peak disappears after OER CP based on XPS results. The disappearance of this peak is attributed to the leaching of Mo species from the catalyst surface during the OER process. Under the highly oxidative anodic environment, Mo-containing surface sites are susceptible to dissolution, resulting in a significant reduction of surface Mo content, as evidenced by the post OER XPS analysis. As the Mo—N bond originates from the coordination between Mo species and nitrogen-containing sites, the removal of Mo certainly disrupts this bonding environment, leading to the disappearance of the corresponding Mo—N signal in the N 1s spectrum, as evidenced in Figure 6d. The disappearance of Mo—N coordination further supports Mo leaching during electrochemical activation [61]. Additionally, the C 1s XPS spectrum of MoO_2/Fe_3O_4-Mel before and after CP (Figure S11) displays a noticeable shift in the main peak, indicating electronic structure modulation induced by electrochemical reconstruction [62]. The survey XPS spectrum of MoO_2/Fe_3O_4-Mel@NF after CP (Figure S12) shows significant variation in elemental peak intensities compared with the pristine catalyst, further confirming surface chemical evolution during OER operation.

To further elucidate the OER reaction pathway, LSV measurements were conducted at different pH values (12–14) using $MoO_{2(0.3)}/Fe_3O_4$-$Mel_{(2)}$@NF (Figure 6e). The relationship between current density and pH reveals weak pH dependence ($\rho^{RHE} \approx 0.55$), indicating that the OER predominantly follows an adsorbate evolution mechanism (AEM) (Figure 6f) [63]. To distinguish between AEM and lattice oxygen-mediated mechanisms (LOM), TMA^+, which strongly interacts with peroxide (O_2^{2-}) intermediates characteristic of LOM pathways, was introduced as a chemical

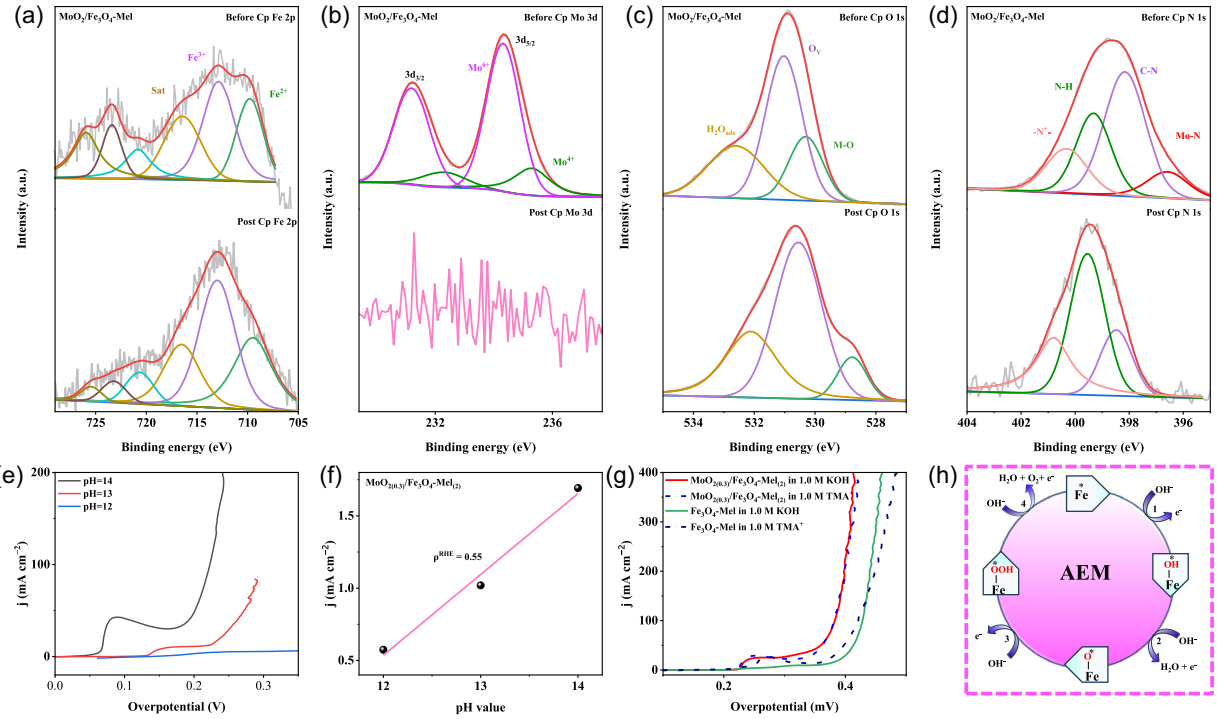

FIGURE 6 | Comparison of XPS spectra of (a) Fe 2p for $MoO_{2(0.3)}/Fe_3O_4$-$Mel_{(2)}$@NF before and after CP. (b) Mo 3d XPS spectrum before and after CP. (c) O 1s XPS spectrum before and after CP. (d) N 1s XPS spectrum before and after CP. (e) pH-dependent OER activity of $MoO_{2(0.3)}/Fe_3O_4$-$Mel_{(2)}$@NF. (f) current densities as a function of pH for $MoO_{2(0.3)}/Fe_3O_4$-$Mel_{(2)}$@NF at 0.2 V versus RHE. (g) Comparison of LSV curves for $MoO_{2(0.3)}/Fe_3O_4$-$Mel_{(2)}$@NF and Fe_3O_4-Mel_2@NF in 1 M KOH and 1 M TMAOH electrolytes. (h) Schematic illustration of AEM pathway.

probe [64]. The presence of TMA^+ does not significantly suppress OER activity, thereby excluding dominant LOM contribution and supporting an AEM-dominated pathway on the reconstructed FeOOH surface. Furthermore, comparative LSV measurements performed in 1 M KOH and 1 M TMAOH electrolytes (Figure 6g) reveal nearly identical catalytic activity for $MoO_{2(0.3)}/Fe_3O_4$-$Mel_{(2)}$@NF. This observation suggests that bulky TMA^+ cations do not significantly influence OH^- adsorption or availability at the catalyst interface [65]. The minimal cation-dependent variation in activity indicates that surface-bound intermediates primarily govern OER kinetics rather than electrolyte-specific ion-pairing effects, further supporting the AEM pathway.

Combined *operando* spectroscopic investigations, post-OER XPS analyses, and chemical probing collectively confirm that the OER process on $MoO_{2(0.3)}/Fe_3O_4$-$Mel_{(2)}$@NF proceeds via oxygen vacancy-modulated surface reconstruction of FeOOH active phases. Oxygen vacancies serve as preferential adsorption centers for OH^- species, enhance interfacial charge transfer, and stabilize critical oxygenated intermediates (*OH to *O and *OOH), thereby accelerating O—O bond formation and oxygen evolution (Figure 6h). It also suggests that FeOOH species generated during OER reaction are the dominant active phase for OER. Nevertheless, the underlying MoO_2 and melamine framework remain crucial for maintaining catalytic performance. MoO_2 serves as a conductive backbone facilitating rapid electron transport and stabilizing the reconstructed FeOOH layer through interfacial interactions, while melamine framework provides structural integrity during long-term operation. In addition, these components promote the formation and stabilization of oxygen vacancies, which regulate the electronic structure of FeOOH and optimize the adsorption of oxygenated intermediates. This synergistic integration of conductive MoO_2 domains, vacancy-rich domains of Fe_3O_4, and the melamine framework is the basis of the high catalytic activity and long-term durability. These findings establish oxygen vacancy-assisted AEM as the dominant OER pathway for the $MoO_{2(0.3)}/Fe_3O_4$-$Mel_{(2)}$@NF catalyst.

2.5 | Overall Water Splitting

A two-electrode electrolyzer configuration was assembled, as illustrated in Figure 7a, using $MoO_{2(0.3)}/Fe_3O_4$-$Mel_{(2)}$ grown on Ni foam as the anode and commercial Pt/C as the cathode to construct an integrated system for evaluating both catalytic activity and operational stability. This configuration enables efficient oxygen evolution at the anode and hydrogen evolution at the cathode, thereby facilitating overall water splitting. For comparison, a reference electrolyzer consisting of RuO_2 as the anode and Pt/C as the cathode ($RuO_2^{(+)}||Pt/C^{(-)}$) was tested under identical conditions. As shown in the LSV curves (Figure 7b), the $MoO_{2(0.3)}/Fe_3O_4$-$Mel_{(2)}^{(+)}||Pt/C^{(-)}$ electrolyzer achieves a low cell voltage of 1.45 V at 100 mA cm^{-2}, significantly outperforming the RuO_2-based reference system, which requires 1.60 V under the same operating conditions. Moreover, the $MoO_{2(0.3)}/Fe_3O_4$-$Mel_{(2)}$-based electrolyzer maintains superior performance across a wide current density range, requiring only 1.53 and 1.63 V to achieve 200 and 400 mA cm^{-2}, respectively (Figure 7c). These results indicate rapid reaction kinetics and reduced energy losses, particularly under high current density conditions that are relevant to industrial electrolysis applications.

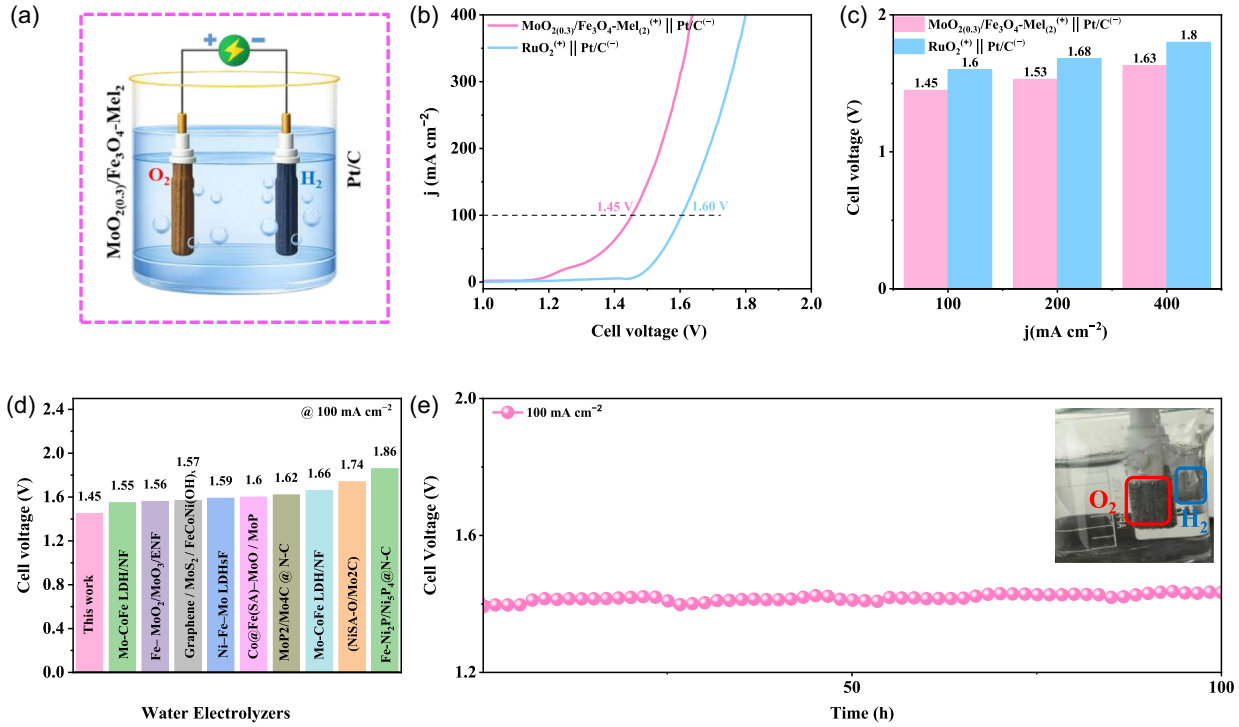

FIGURE 7 | Overall water-splitting (OWS) performance of $MoO_{2(0.3)}/Fe_3O_4$-$Mel_{(2)}$. (a) Schematic illustration of the overall water-splitting process in a two-electrode configuration. (b) Polarization (LSV) curves for OWS of the $MoO_{2(0.3)}/Fe_3O_4$-$Mel_{(2)}^{(+)}$‖$Pt/C^{(-)}$ electrolyzer and $RuO_2^{(+)}$‖$Pt/C^{(-)}$ in 1.0 M KOH. (c) Comparison of the cell voltages required to reach different current densities for the $MoO_{2(0.3)}/Fe_3O_4$-$Mel_{(2)}^{(+)}$‖$Pt/C^{(-)}$ and $RuO_2^{(+)}$‖$Pt/C^{(-)}$ electrolyzers. (d) Comparison of the OWS performance of the $MoO_{2(0.3)}/Fe_3O_4$-$Mel_{(2)}$-based electrolyzer with previously reported water splitting catalysts. (e) Long term durability evaluation conducted by chronopotentiometry at 100 mA cm^{-2} for 100 h (inset: photograph of the electrolyzer during the stability test).

Performance comparison with previously reported catalysts further highlights the advantages of the $MoO_{2(0.3)}/Fe_3O_4$-$Mel_{(2)}^{(+)}$‖$Pt/C^{(-)}$ configuration. As summarized in Figure 7d and Table S2, the developed electrolyzer demonstrates competitive performance among noble metal-free electrocatalysts, particularly at elevated current densities. In addition to its high catalytic activity, the assembled electrolyzer exhibits excellent long-term durability. The system sustains stable operation at 100 mA cm^{-2} for 100 h with negligible voltage decay (Figure 7e), demonstrating strong electrochemical stability and resistance to degradation during continuous alkaline water electrolysis. The exceptional durability can be attributed to the robust composite architecture, synergistic Mo—Fe electronic interactions, and oxygen vacancy-stabilized active sites that maintain efficient charge transfer and structural integrity under prolonged operation. Overall, the $MoO_{2(0.3)}/Fe_3O_4$-$Mel_{(2)}$ catalyst exhibits excellent intrinsic activity and durability for overall water splitting, effectively lowering the energy requirement for oxygen evolution and highlighting its strong potential for practical alkaline electrolysis applications.

3 | Conclusion

In conclusion, we successfully developed a vacancy-engineered MoO_2/Fe_3O_4-Mel nanorod composite as a highly efficient and durable precatalyst for alkaline oxygen evolution. The logical integration of conductive MoO_2 domains, Fe-based redox active centers, and a nitrogen-rich melamine framework results in strong interfacial coupling, increased oxygen vacancy generation, and improved electronic modulation of catalytically active sites. The optimized $MoO_{2(0.3)}/Fe_3O_4$-$Mel_{(2)}$ catalyst delivers outstanding OER performance, achieving low overpotentials of 217 mV at 100 mA cm^{-2} and 259 mV at 300 mA cm^{-2}, along with fast reaction kinetics reflected by a low Tafel slope of 70 mV dec^{-1} and superior mass activity of 77.33 A g^{-1}. In situ Raman and in situ FTIR analyses reveal dynamic surface reconstruction into FeOOH active phases and confirm that oxygen vacancies facilitate OH^- adsorption, stabilize reaction intermediates, and accelerate electron transfer, encouraging an OER pathway driven by AEM. The catalyst demonstrates excellent electrochemical stability, sustaining stable operation for 150 h at 100 mA cm^{-2}, showing the structural robustness of the composite. Furthermore, practical water splitting evaluation in a two-electrode electrolyzer configuration yields a low cell voltage of 1.45 V at 100 mA cm^{-2} and stable long-term operation, exceeding RuO_2 based reference systems. These findings demonstrate that oxygen vacancy-assisted electronic modulation and controlled precatalyst reconstruction serve as effective design approaches for developing next-generation, noble metal-free electrocatalysts for efficient, scalable alkaline water electrolysis.

4 | Experimental Section

4.1 | Materials

Iron(III) nitrate nonahydrate ($Fe(NO_3)_3{\cdot}9H_2O$, ≥99%), ethanol (C_2H_5OH, 99.7%), sulfuric acid (H_2SO_4, 37%), and ammonium

heptamolybdate tetrahydrate ($(NH_4)_6Mo_7O_{24}{\cdot}4H_2O$, ≥99%) were procured from Xilong Science Co., Ltd. Melamine ($C_3N_3(NH_2)_3$, 99%) and Ruthenium(III) chloride hydrate ($RuCl_3{\cdot}xH_2O$, 35%–42%) were supplied by Shanghai Aladdin Chemical Reagent Co., Ltd., while potassium hydroxide (KOH, 90%) was purchased from Shanghai Macklin Chemical Reagent Co., Ltd. Commercial platinum on carbon (Pt/C, 20 wt%) and Nafion solution (5 wt%) were obtained from Suzhou Sinero Technology Co., Ltd. RuO_2 powder was prepared by calcining $RuCl_3$ in air at 400 °C. NF, used as the current collector, was purchased from Guang Sheng Jia New Materials Co., Ltd.; the NF sheets with a thickness of 1.6 mm were cut into $2 \times 4\ cm^2$ pieces prior to use. Deionized water was used as solvent and for washing purposes. All reagents were used directly without purification.

4.2 | Synthesis of Fe_3O_4-Mel@NF

NF ($2 \times 4\ cm^2$) was ultrasonically cleaned in 0.5 M H_2SO_4, ethanol, and deionized water, respectively. Each step was carried out for 15 mins to remove surface impurities and obtain a clean substrate. Then, to synthesize Fe_3O_4-Mel, Iron(III) nitrate nonahydrate (1 mM, $Fe(NO_3)_3{\cdot}9H_2O$) and melamine (2 mM) were dissolved in a mixed solvent of deionized water (25 mL) and ethanol (25 mL). The solution was sonicated for 20 min, after which the homogeneous mixture was transferred into a Teflon-lined stainless-steel autoclave containing precleaned NF ($2 \times 4\ cm^2$). The autoclave was sealed and heated at 180 °C for 8 h. After naturally cooling to room temperature, the NF was thoroughly rinsed with deionized water and ethanol, then dried at 60 °C.

4.3 | Synthesis of MoO_2/Fe_3O_4-Mel@NF

To synthesize MoO_2/Fe_3O_4-Mel, Iron(III) nitrate nonahydrate (1 mM, $Fe(NO_3)_3{\cdot}9H_2O$) and melamine (2 mM) were dissolved in a mixed solvent of deionized water (15 mL) and ethanol (15 mL). Separately, ammonium heptamolybdate tetrahydrate ($(NH_4)_6Mo_7O_{24}{\cdot}4H_2O$, 0.3 mM) was dissolved in 20 mL of deionized water. The two solutions were combined and sonicated for 20 min, after which the homogeneous mixture was transferred into a Teflon-lined stainless-steel autoclave containing precleaned NF ($2 \times 4\ cm^2$). The autoclave was sealed and heated at 180 °C for 8 h. After naturally cooling to room temperature, the NF was thoroughly rinsed with deionized water and ethanol, followed by drying at 60 °C. To investigate the effect of molybdate concentration, ammonium heptamolybdate tetrahydrate was varied to 0.1, 0.2, 0.3, and 0.4 mM, while keeping all other parameters unchanged. For melamine optimization, its concentration was adjusted to 1, 2, and 3 mM, with the ammonium heptamolybdate concentration fixed at 0.3 mM.

Furthermore, the total amount of $Fe(NO_3)_3{\cdot}9H_2O$ was kept constant at 1 mmol, while the amount of melamine and $(NH_4)_6Mo_7O_{24}{\cdot}4H_2O$ was varied proportionally to prepare a series of samples. All the samples were synthesized using the same procedure, and the resulting catalysts were labelled as $MoO_{2(0.1)}/Fe_3O_4$-$Mel_{(2)}$, $MoO_{2(0.2)}/Fe_3O_4$-$Mel_{(2)}$, $MoO_{2(0.3)}/Fe_3O_4$-$Mel_{(2)}$, $MoO_{2(0.4)}/Fe_3O_4$-$Mel_{(2)}$, $MoO_{2(0.3)}/Fe_3O_4$-$Mel_{(1)}$, and $MoO_{2(0.3)}/Fe_3O_4$-$Mel_{(3)}$.

4.4 | Synthesis of RuO_2@NF and Pt/C@NF Electrodes

To compare RuO_2 and Pt/C catalysts, the coating solution was prepared separately by dispersing 2 mg of RuO_2 and 20 wt% Pt/C each into a mixture of 200 μL deionized water, 200 μL ethanol, and 5 μL of a 5 wt% Nafion solution. The resultant mixture was sonicated for 30 min to produce a homogeneous suspension. The solution were separately drop-coated onto a spotless NF substrate measuring 1 cm × 1 cm and then dried in air at ambient conditions.

Author Contributions

Rahmat Ullah: writing – original draft, investigation, methodology, conceptualization. **Jinshan Cheng:** writing – review & editing, formal analysis. **Sheraz Muhammad:** writing – review & editing, investigation, data curation. **Sumayya Khan:** data curation. **Huaifeng Li:** methodology & formal analysis. **Ali Aman:** formal analysis. **Ke Zhang:** methodology. **Tayirjan Taylor Isimjan:** writing – review & editing. **Shohreh Azizi:** writing – review & editing. **Xiulin Yang:** writing – review & editing, supervision.

Acknowledgments

This work was financially supported by the Guangxi Science and Technology Projects (GUIKE LT2600640010), the Natural Science Foundation of Guangxi Province (2026GXNSFBA00640178), and the National Natural Science Foundation of China (52363028; W2621022; 21965005).

Funding

This study was supported by National Natural Science Foundation of China (52363028; W2621022; 21965005), Natural Science Foundation of Guangxi Province (2026GXNSFBA00640178), Guangxi Science and Technology Projects (GUIKE LT2600640010).

Conflicts of Interest

The authors declare no conflicts of interest.

Data Availability Statement

Data will be made available on request.

References

1. A. Y. Goren, I. Dincer, and A. Khalvati, "A Comprehensive Life Cycle Impact Evaluation of Hydrogen Production Processes for Cleaner Applications," *Energy* 326 (2025): 136182.

2. X. Li, T. Wu, N. Li, et al., "Vertically Staggered Porous Ni_2P/Fe_2P Nanosheets With Trace Ru Doping as Bifunctional Electrocatalyst for Alkaline Seawater Splitting," *Advanced Functional Materials* 34 (2024): 2400734.

3. H. Zhao, Z. Li, S. Zhou, et al., "Phosphate Anion as Dynamic Proton Modulator for Efficient Hydrogen Evolution in Alkaline Media," *Advanced Functional Materials* 36 (2026): e31507.

4. Q. Qian, Y. Zhu, N. Ahmad, et al., "Recent Advancements in Electrochemical Hydrogen Production via Hybrid Water Splitting," *Advanced Materials* 36 (2024): 2306108.

5. S. Hua, S. A. Shah, G. E. O. Nsang, et al., "Unveiling Active Sites in FeOOH Nanorods@ NiOOH Nanosheets Heterojunction for Superior

OER and HER Electrocatalysis in Water Splitting," *Journal of Colloid and Interface Science* 679 (2025): 487–495.

6. B. Li, F. Deng, H. Wang, Z. Li, F. Yan, and C. Yu, "Core-Shell Quantum Wires-Supported Single-Atom Fe Electrocatalysts for Efficient Overall Water Splitting," *Small* 21 (2025): 2409542.

7. S. Muhammad, L. Wang, Z. Huang, et al., "Recent Advances in Lanthanide-Based Materials for Oxygen Evolution Reaction: Challenges and Future Prospects," *Coordination Chemistry Reviews* 534 (2025): 216573.

8. M. Tsipoaka and A. A. Rownaghi, "Toward Understanding the Stability of Single-Atom Catalysts in Oxygen Evolution Reactions," *Advanced Energy Materials* 15 (2025): 2500635.

9. I. Fareed, M. D. Khan, M. Firdous, et al., "Fundamentals and Perspectives on Materials for Bifunctional Electrocatalysis," *Advanced Science* 12 (2025): e09902.

10. W. Zhang, L. Yang, Z. Li, et al., "Regulating Hydrogen/Oxygen Species Adsorption via Built-in Electric Field-Driven Electron Transfer Behavior at the Heterointerface for Efficient Water Splitting," *Angewandte Chemie* 136 (2024): e202400888.

11. Q. Yu, Y. Fu, Z. Liu, et al., "Regulating Local Atomic Environment of Fe_3O_4 to Promote Anion Exchange Membrane Based Alkaline Seawater Electrolysis," *Applied Catalysis B: Environment and Energy* 361 (2025): 124598.

12. D. Khalafallah, L. Feng, Z. Sun, S. Tong, J. Wang, and Q. Zhang, "Advanced Fe Electrocatalysts: Unlocking Sustainable, Selective, and Durable Seawater Electrolysis," *Advanced Functional Materials* 35 (2025): 2506186.

13. L. Hou, J. Sun, C. Sun, et al., "Multi-Heterogeneous Interfaces Modulation of $NiO/MoO_3/Fe_2O_3$ for Enhanced Water/Seawater Splitting," *Advanced Sustainable Systems* 9 (2025): e00495.

14. Q. Xu, J. Zhang, H. Zhang, et al., "Atomic Heterointerface Engineering Overcomes the Activity Limitation of Electrocatalysts and Promises Highly-Efficient Alkaline Water Splitting," *Energy and Environmental Science* 14 (2021): 5228–5259.

15. X. Chen, H. Su, T. Li, I. Lynch, H. Zhang, and R. Zou, "Structural and Interfacial Design of Atomically Thin Materials and Their Heterostructures for Advancing Electrocatalysis," *Advanced Materials* 38 (2026): e15722.

16. Q. Zhang, Y. Dou, C. Liu, et al., "Vacancy Engineering Strategies for Water Splitting Electrocatalysts," *Electrochemical Energy Reviews* 8 (2025): 36.

17. X. Du, J. Zhang, X. Zhou, et al., "Boosting the Efficient Alkaline Seawater Oxygen Evolution Reaction of Iron Oxide Hydroxide via Plasma-Induced Oxygen Defect Engineering," *Green Chemistry* 27 (2025): 3515–3523.

18. R. M. Bhattarai, L. Nguyen, N. Le, et al., "Cyanide Functionalization and Oxygen Vacancy Creation in Ni-Fe Nano Petals Sprinkled With MIL-88A Derived Metal Oxide Nano Droplets for Bifunctional Alkaline Seawater Electrolysis," *Small* 21 (2025): 2410027.

19. H. L. Andersen, C. Granados-Miralles, K. M. Jensen, et al., "The Chemistry of Spinel Ferrite Nanoparticle Nucleation, Crystallization, and Growth," *ACS Nano* 18 (2024): 9852–9870.

20. L. G. Graversen, M. Juelsholt, O. Aalling-Frederiksen, et al., "Mechanistic Insights Into Solvent-Guided Growth and Structure of MoO_2 Nanoparticles in Solvothermal Synthesis," *Chemical Science* 16 (2025): 14350–14365.

21. B. Ma, W. Hao, W. Ruan, et al., "Unveiling Capacitive Behaviors of MoO_2 in Different Electrolytes and Flexible MoO_2-Based Asymmetric Micro-Supercapacitor," *Journal of Energy Storage* 52 (2022): 104833.

22. P. Qin, D. Yi, J. Hao, X. Ye, M. Gao, and T. Song, "Fabrication of Melamine Trimetaphosphate 2D Supermolecule and Its Superior Performance on Flame Retardancy, Mechanical and Dielectric Properties of Epoxy Resin," *Composites Part B: Engineering* 225 (2021): 109269.

23. M. A. Ahmed, A. Toghan, M. A. Ahmed, and A. A. Mohamed, "Synergistic Adsorption-Photocatalysis via rGO-Mediated Electron Shuttling in Ultrasonically Synthesized NiO/gC_3N_4-Based Ternary Nanocomposites for Safranin O Removal," *RSC Advances* 15 (2025): 47520–47544.

24. R. Abazari, Z. A. Torkamani, A. Ejsmont, et al., "Interfacial Engineering of Pillared Co (II) Metal–organic Framework@ NiMn-Layered Double Hydroxide Nanocomposite for Oxygen Evolution Reaction Electrocatalysis," *Inorganic Chemistry* 64 (2025): 361–370.

25. B. Zhou, H. Ye, Y. Li, et al., "In-Situ Co-Growth of 2D/1D g-C_3N_4/a-WO_x Amorphous Heterojunctions for Near-Infrared-Driven Photocatalytic Hydrogen Evolution," *Separation and Purification Technology* 372 (2025): 133455.

26. X. Tao, L. Hou, X. Wang, J. Jin, H. Li, and F. Gao, "Iron and Oxygen Vacancies Co-Modulated Adsorption Evolution and Lattice Oxygen Dual-Path Mechanism for Water Oxidation," *Nature Communications* 16 (2025): 8788.

27. F. Xie, Z. Yuan, L. Feng, et al., "Unveiling the Non-Catastrophic Oxidation Mechanism of High Molybdenum Carbon-Free High-Speed Steel Using Multi-Scale Characterization," *Materials Characterization* 228 (2025): 115425.

28. K. S. Kim, J. Byeon, A. R. Koirala, H. Kim, J. Lee, and D. C. Lee, "Deposition of Fe_3O_4 Overlayers on Nickel-Anchored Molybdenum Oxide for Enhanced and Stable Oxygen Evolution Reaction in Alkaline Water Electrolysis," *Inorganic Chemistry Frontiers* 12 (2025): 7760–7774.

29. X. Ji, Y. Lin, J. Zeng, et al., "Graphene/MoS_2/FeCoNi$(OH)_x$ and Graphene/MoS_2/FeCoNiP_x Multilayer-Stacked Vertical Nanosheets on Carbon Fibers for Highly Efficient Overall Water Splitting," *Nature Communications* 12 (2021): 1380.

30. N. F. Agesta, Y.-L. Woo, J. Y. Loh, F. M. Yap, X. Zeng, and W.-J. Ong, "Temperature-Driven Phase Engineering: Synergistic Effect Between NiS_2 and MoS_2 Coupled With N-Doped Graphene Self-Supported on Carbon Cloth for Efficient Electrocatalytic Seawater Splitting," *Journal of Materials Chemistry a* 13 (2025): 40213–40228.

31. Y. Gao, Z. Li, M. Deng, et al., "Anchoring Ni Nanoparticles on MoO_2 Nanorods for Enhancing Electrocatalytic Oxidation of Glycerol to Formate," *Colloids and Surfaces a-Physiochemical and Engineering Aspects* 715 (2025): 136661.

32. X. Song, Y. Ren, W. Qin, H. Wang, Y. Zeng, and M. Li, "Double MOF Derived $Co_2Mo_3O_8$-MoO_2 Nanorod Cluster Heterostructure as Separator-Mediator for High Performance Lithium-Sulfur Batteries," *Journal of Alloys and Compounds* 1062 (2026): 187561.

33. S. Wang, Y. Ke, F. Jin, Y. Li, and Z. Jin, "The Built-in Electric Field Regulates the d-Band Center of the $FeCo_2O_4$/ZnCdS Heterojunction to Enhance Photocatalytic Hydrogen Evolution," *ChemSusChem* 18 (2025): e202500950.

34. J. Jia, Y. Wang, Y. Cha, et al., "Boosting OER Performance of NiFe-MOFs via Heterostructure Engineering: Promoted Phase Transformation and Self-Optimized Dynamic Interface Electron Structure," *Advanced Functional Materials* 35 (2025): 2500568.

35. S. Muhammad, L. Wang, M. Gao, et al., "Fe-Ce Interaction-Driven Active Site Modulation in a Porous MOF for Oxygen Evolution Reaction," *Fuel* 405 (2026): 136782.

36. H. Zhu, Y. Liu, A. Wu, et al., "Nanosheet-Based 3-Dimentional Assembly With Synergitic Co-Mo Sites for Effective Electrocatalytic Hydrogen Evolution Reaction," *Chemical Engineering Journal* 510 (2025): 161490.

37. T. Tang, Y. Chen, K. Sun, et al., "Engineering Mn-Doped Co-Based Heterostructures With Oxygen Vacancies Toward Efficient

Industrial-Scale Water Oxidation Catalysis," *Journal of Colloid and Interface Science* 690 (2025): 137314.

38. P. Hu, F. F. Yang, F. Yang, et al., "Bimetallic Organic Framework Derived Co-Mo_xN/Mo_2C Catalyst for HER/OER Bifunctional Electrocatalytic Reaction," *Journal of Colloid and Interface Science* 680 (2025): 427–436.

39. Y. Du, Z. Zhong, Z. Shi, et al., "Dual-Ligand Engineered CoNi Alloy/N-Doped Carbon Nanotubes Bifunctional ORR/OER Electrocatalyst for Long-Lifespan Rechargeable Zn-Air Batteries," *Journal of Colloid and Interface Science* 683 (2025): 631–640.

40. S. Muhammad, B. Yao, A. Zhou, et al., "Unveiling Dynamic Surface Transformations: Mo-Doped Fe-Based MOFs as Next-Generation Oxygen Evolution Catalysts," *Green Chemistry* 27 (2025): 5554–5566.

41. M. Xi, Z. Wu, Z. Luo, et al., "Water Activation for Boosting Electrochemiluminescence," *Angewandte Chemie International Edition* 62 (2023): e202302166.

42. T. Tang, Y. Teng, K. Sun, et al., "Self-Etching Synthesis of Superhydrophilic Iron-Rich Defect Heterostructure-Integrated Catalyst With Fast Oxygen Evolution Kinetics for Large-Current Water Splitting," *ChemSusChem* 18 (2025): e202401872.

43. A. P. Hegde, P. Mukesh, G. Lakshmisagar, et al., "Melamine–Ni-MIL-88A Blend Derived Trevorite/Cg-C_3N_4 for Stable and Efficient Overall Electrocatalytic Water Splitting Applications," *Journal of Alloys and Compounds* 1031 (2025): 180649.

44. J. Liu, L. Cao, H. Ma, et al., "Modulated Selectivity in Oxygen Reduction for FeMn-Based Melamine Framework via Differential Pyrolysis," *Journal of Colloid and Interface Science* 701 (2026): 138693.

45. P. Wu, S. Geng, X. Wang, et al., "Exfoliation of Metal–organic Frameworks to Give 2D MOF Nanosheets for the Electrocatalytic Oxygen Evolution Reaction," *Angewandte Chemie International Edition* 63 (2024): e202402969.

46. J. Mu, C. Yu, X. Song, L. Chen, J. Zhao, and J. Qiu, "A Super-Chlorophobic Yet Weak-Reconstructed Electrocatalyst by Fluorination Engineering Toward Chlorine Oxidation-Free and High-Stability Seawater Electrolysis," *Advanced Functional Materials* 35 (2025): 2423965.

47. M. Gao, W. Pan, Z. Huang, et al., "Electron Transfer Enhanced Flower-Like NiP_2-Mo_8P_5 Heterostructure Synergistically Accelerates Fast HER Kinetics for Large-Current Overall Water Splitting," *Journal of Colloid and Interface Science* 683 (2025): 1087–1095.

48. F. Wei, J. Shen, J. Xie, et al., "Dynamic In Situ Reconstruction of $NiSe_2$ Promoted by Interfacial $Ce_2(CO_3)_2O$ for Enhanced Water Oxidation," *Journal of Energy Chemistry* 98 (2024): 472–480.

49. Y. Chen, C. Guo, Y. Wang, K. Wang, and S. Song, "Constructing High-Entropy Spinel Oxide Thin Films via Magnetron Sputtering for Efficiently Electrocatalyzing Alkaline Oxygen Evolution Reaction," *Chinese Journal of Catalysis* 77 (2025): 210–219.

50. S. Zhang, Z. Huang, T. T. Isimjan, D. Cai, and X. Yang, "Accurately Substituting Fe for Ni_2 Atom in Ni-MOF With Defect-Rich for Efficient Oxygen Evolution Reaction: Electronic Reconfiguration and Mechanistic Study," *Applied Catalysis B: Environment and Energy* 343 (2024): 123448.

51. S. Liu, L. Wang, H. Jang, et al., "Dynamic Water Network Reconfiguration via Oxyphilic V Dopants Enables Industrial-Current-Density Alkaline Hydrogen Evolution," *Science China Chemistry* 69 (2026): 2416–2424.

52. Y. Wang, J. Han, W. Bao, et al., "Unveiling How Reconstructed Molybdenum Oxyanions Enhances the Alkaline Oxygen Evolution Reaction," *Chemical Engineering Journal* 518 (2025): 164835.

53. S. Zuo, Z. P. Wu, G. Zhang, et al., "Correlating Structural Disorder in Metal (oxy) Hydroxides and Catalytic Activity in Electrocatalytic Oxygen Evolution," *Angewandte Chemie International Edition* 63 (2024): e202316762.

54. Z. Wang, Q. Zhou, L. Luo, et al., "Suppressing Catalyst Reconstruction in Neutral Electrolyte: Stabilizing Co-O-Mo Point-to-Point Connection of Cobalt Molybdate by Tungsten Doping for Oxygen Evolution Reaction," *Chinese Journal of Catalysis* 76 (2025): 146–158.

55. X. Li, J. Wang, H. Xue, et al., "Tuning α-MnOOH Formation via Atomic-Level Fe Introduction for Superior OER Performance," *Advanced Functional Materials* 35 (2025): 2503360.

56. S. Muhammad, H. Sun, S. Zahoor, et al., "Advancing MOFs for Electrocatalytic ORR, UOR, and CO_2RR: From Fundamentals to Device Integration and Deployment Challenges," *Materials Science and Engineering R: Reports* 171 (2026): 101248.

57. Y. Huang, Z. Gu, J. Wang, et al., "Boosting Oxygen Evolution Reaction Activity and Durability of FeOOH-MOF Composite at Industrial-Grade Current Densities by a Facile Corrosion Strategy," *Applied Catalysis B- Environment and Energy* 371 (2025): 125221.

58. X. Luo, H. Zhao, X. Tan, et al., "Fe-S Dually Modulated Adsorbate Evolution and Lattice Oxygen Compatible Mechanism for Water Oxidation," *Nature Communications* 15 (2024): 8293.

59. X. Wang, W. Zhou, S. Zhai, et al., "Metal-Organic Frameworks: Direct Synthesis by Organic Acid-Etching and Reconstruction Disclosure as Oxygen Evolution Electrocatalysts," *Angewandte Chemie* 136 (2024): e202400323.

60. X. Fu, J. Yu, H. Li, et al., "Fe Ion Doping as an Effective Strategy to Enhance Oxygen Evolution Reaction Activity in $NiCo_2O_4$," *Journal of Power Sources* 630 (2025): 236159.

61. K. Zeng, Y. Li, M. Tian, et al., "Molybdenum-Leaching Induced Rapid Surface Reconstruction of Amorphous/Crystalline Heterostructured Trimetal Oxides Pre-Catalyst for Efficient Water Splitting and Zn-Air Batteries," *Energy Storage Materials* 60 (2023): 102806.

62. M. Zhu, P. Tang, X. Li, et al., "Interface Engineering of $NiSe_2$/$FeSe_2$ Derived From Metal-Organic Framework as a Bifunctional Catalyst for Efficient UOR and OER," *International Journal of Hydrogen Energy* 102 (2025): 626–634.

63. F. Wu, F. Tian, M. Li, et al., "Engineering Lattice Oxygen Regeneration of NiFe Layered Double Hydroxide Enhances Oxygen Evolution Catalysis Durability," *Angewandte Chemie International Edition* 64 (2025): e202413250.

64. H. Yin, M. Huang, L. Wang, et al., "Lattice-Mismatched MOF-on-MOF Nanosheets With Rich Oxygen Vacancies Show Fast Oxygen Evolution Kinetics for Large-Current Water Splitting," *Applied Catalysis B: Environment and Energy* 367 (2025): 125105.

65. H. Song, X. Yong, G. I. Waterhouse, et al., "RuO_2-CeO_2 Lattice Matching Strategy Enables Robust Water Oxidation Electrocatalysis in Acidic Media via Two Distinct Oxygen Evolution Mechanisms," *ACS Catalysis* 14 (2024): 3298–3307.

Supporting Information

Additional supporting information can be found online in the Supporting Information section.